Medical Image Analysis 51 (2019) 144–156

Contents lists available at ScienceDirect

Medical Image Analysis

journal homepage: www.elsevier.com/locate/media

Recovery of 3D rib motion from dynamic chest radiography and CT data using local contrast normalization and articular motion model

Yuta Hiasa[a,*], Yoshito Otake[a], Rie Tanaka[b], Shigeru Sanada[b], Yoshinobu Sato[a]

[a] Graduate School of Information Science, Nara Institute of Science and Technology, Japan
[b] Department of Quantum Medical Technology, Kanazawa University, Japan

ARTICLE INFO

Article history:
Received 23 January 2018
Revised 2 October 2018
Accepted 18 October 2018
Available online 19 October 2018

Keywords:
2D–3D registration
Rib motion analysis
Articular motion model
Local contrast normalization

ABSTRACT

Dynamic chest radiography (2D x-ray video) is a low-dose and cost-effective functional imaging method with high temporal resolution. While the analysis of rib-cage motion has been shown to be effective for evaluating respiratory function, it has been limited to 2D. We aim at 3D rib-motion analysis for high temporal resolution while keeping the radiation dose at a level comparable to conventional examination. To achieve this, we developed a method for automatically recovering 3D rib motion based on 2D-3D registration of x-ray video and single-time-phase computed tomography. We introduce the following two novel components into the conventional intensity-based 2D–3D registration pipeline: (1) a rib-motion model based on a uniaxial joint to constrain the search space and (2) local contrast normalization (LCN) as a pre-process of x-ray video to improve the cost function of the optimization parameters, which is often called the *landscape*. The effects of each component on the registration results were quantitatively evaluated through experiments using simulated images and real patients' x-ray videos obtained in a clinical setting. The rotation-angle error of the rib and the mean projection contour distance (mPCD) were used as the error metrics. The simulation experiments indicate that the proposed uniaxial joint model improved registration accuracy. By searching the rotation axis along with the rotation angle of the ribs, the rotation-angle error and mPCD significantly decreased from $2.246 \pm 1.839°$ and 1.148 ± 0.743 mm to $1.495 \pm 0.993°$ and 0.742 ± 0.281 mm, compared to simply applying De Troyer's model. The real-image experiments with eight patients demonstrated that LCN improved the cost function space; thus, robustness in optimization resulting in an average mPCD of 1.255 ± 0.615 mm. We demonstrated that an anatomical-knowledge based constraint and an intensity normalization, LCN, significantly improved robustness and accuracy in rib-motion reconstruction using chest x-ray video.

1. Introduction

The rib cage, lungs, and thoracic muscles cooperatively contribute to the pulmonary function. Since the rib cage mobility is a key factor in the respiratory motion partly in relation with spine deformity, analysis of the rib cage motion has received considerable attention and its importance was pointed out especially on the patients with chronic obstructive pulmonary disease (COPD) (Gilmartin and Gibson, 1986), kyphosis (Culham et al., 1994), scoliosis (Tanaka et al., 2015), and so on. Clinically available systems for accurate rib cage motion analysis are required for diagnosis of these patients. In the biomechanics research field, three-dimensional (3D) modeling of the rib cage and muscles has been addressed to analyze the rib cage and muscular biomechanics (Didier et al., 2009; Bruno et al., 2015). In vivo 3D imaging techniques of the rib cage motion will be useful for its patient-specific adaptation.

The ribs are main targets for motion analysis in the rib cage due to its movability during the respiratory motion. Two clinical imaging approaches have been proposed for the rib motion analysis. One is multi-phase CT imaging (Beyer et al., 2014) and the other is dynamic chest radiography (Tanaka et al., 2015). The former method can directly acquire 3D transformation parameters between two time phases of the rib motion, however, increasing time resolution or follow-up examination is difficult due to the amount of patient dose. The latter has an advantage of high temporal resolution, but it has been limited to 2D. In this work, we combine modalities used in the two approaches to formulate a method for recovering 3D rib motion with high temporal resolution while min-

* Corresponding author.
E-mail addresses: hiasa.yuta.ht7@is.naist.jp (Y. Hiasa), otake@is.naist.jp (Y. Otake), yoshi@is.naist.jp (Y. Sato).

https://doi.org/10.1016/j.media.2018.10.002
1361-8415/

imizing increase of radiation dose, which is based on 2D–3D registration of dynamic chest radiography and a single-time-phase CT.

2D–3D registration has been utilized in a number of applications to 3D pose estimation of skeletal structures from 2D radiographs (Markelj et al., 2012). Compared with other typical skeletal x-ray images, the edge detection and labeling of individual bones in the chest radiography are troublesome because other bones (e.g., scapula, clavicle, and sternum) and soft tissues including blood vessels inside the lungs are superimposed, and several ribs are arranged in parallel making anatomical correspondences ambiguous. Therefore, we also need to consider a method to facilitate automation in extraction and recognition of the edges of the ribs used for 2D–3D registration.

1.1. Related work

Dynamic chest radiography based on an x-ray video system with a flat panel detector is expected to be a low-dose and cost-effective functional imaging method for evaluating pulmonary function (Tanaka, 2016). A recent report (Tanaka et al., 2015) demonstrated the usefulness of rib-motion analysis using two-dimensional (2D) optical flows in the x-ray video to evaluate the respiratory function of scoliotic patients. Although time-varying information was effectively used, its analysis was limited to 2D.

The 3D rib motion was previously analyzed using multi-time-phase CT data acquired at inhale and exhale phases (Ito et al., 2011). However, acquisition of CT at a larger number of time phases to increase temporal resolution requires a larger radiation dose, which limits its applicability in a routine clinical setting. In a broader context, 3D knee-motion analysis at higher temporal resolution was conducted by combining 3D MRI and x-ray video (Chen et al., 2014), where the patient-specific rotational axis of the articular motion was estimated from multiple 3D MRI data of different knee-joint postures to ensure the robustness of 2D–3D registration of the x-ray video and MRI-derived bone models. The necessity of acquiring multiple 3D MRI for estimating the rotational axis is a drawback. Due to its long scan time and artifacts caused by patient motion, this approach is not applicable to anatomies that require large field-of-view (FOV) and move continuously such as the chest region. Computed tomography is commonly acquired for the chest domain in a routine clinical setting; therefore, to avoid an increase in radiation exposure, we attempt to use the single-time-phase CT data.

Static 3D rib analysis based on 2D–3D registration and reconstruction was also addressed in previous work (Dworzak et al., 2010; Grenier et al., 2013). These studies assumed manual extraction and anatomical labeling of the contours or the center lines of the ribs in the x-ray images. Applying these techniques to each frame of the x-ray video would be time-consuming and labor task due to manually extraction.

LCN has been paid more attention by the human/computer vision and neural network communities (Heeger, 1992; Jarrett et al., 2009) rather than medical imaging community, and its effectiveness in face recognition application was investigated (Le, 2013). Although there are a couple of early successful medical applications (Veldkamp and Karssemeijer, 2000; Fleming et al., 2006). Chen et al. (2013) carried out a pre-processing similar to the LCN in 2D–3D registration of carpal bones; however, the detailed formulation of the pre-processing was not given and its effect on the registration results was not investigated.

In the context of evaluation of 2D–3D registration, the quantitative evaluation in experiments using real images is generally not straightforward due to lack of the ground truth. Chen et al. (2014) qualitatively confirmed that the motion pattern of the knee joint estimated from real-image reasonably follows the well-known kinematics of the human knee joint. Villard et al. (2014) evaluated the estimated rib motion indirectly by computing the synchronicity of the motion pattern with diaphragm movement. In this paper, we quantitatively evaluated the rib motion in two steps: validity of the error metric, distance in the projection plane (mPCD), was confirmed by determining its correlation with the actual rotation angle error (Fig. 6(c)), and then by using the validated error metric, we evaluated the method on the real images using manually traced contours as the ground truth.

1.2. Contributions

We propose a method to address the above-mentioned two obstacles, i.e., (1) the rotational-motion constraint modeling and (2) facilitation of automation in edge recognition. The proposed method includes the following two components accordingly: (1) rib-motion model of a uniaxial joint whose axis location is softly constrained by anatomical knowledge to improve robustness while maintaining accuracy, and (2) local contrast normalization (LCN) for pre-processing of x-ray video images to facilitate automation. Unlike the previous medical applications, which aimed at improving performance in feature extraction, we aimed at improving 2D–3D registration using LCN. In this study, for the first time to the best of our knowledge, we demonstrated that LCN actually changed the cost-function space, which results in avoiding failure due to convergence to the local optimum solutions, as clearly shown in Fig. 7.

1.3. Paper organization

The paper is organized as follows. In Section 2, our proposed method is described, including preprocessing of CT and radiography, parameterization of rib motion, DRR generation, similarity metric, initialization of patient position, regularization and optimization, and error metric. In Section 3, we quantitatively evaluated the proposed method through experiments using simulated images and real x-ray videos obtained in a clinical setting. Then, we discuss about our method in Section 4, and conclude this paper in Section 5.

2. Methods

2.1. Overview

Fig. 1 shows the workflow of the proposed method. Local contrast normalization is first applied to the x-ray video, which is used as an input of 2D–3D registration. The algorithm underlying the proposed 2D–3D registration method follows that of Otake et al. (2012, 2015) optimize rigid transformation parameters to maximize the similarity measure between the digitally reconstructed radiograph (DRR) and acquired actual radiograph. We enhanced the algorithm to estimate relative poses of multiple rigid objects connected by joints such as the rib cage. First, we segment each bone in the CT data. Then, using a statistical shape model (SSM), we automatically identify joints on each rib bone to define an initial estimate of the uniaxial rotation axis, which is described in detail in Section 2.4. We formulate the recovery of the rib motion as a problem of estimating a six-degree-of-freedom (DoF) global transformation of the spine and local transformations of each rib with respect to the spine. The motion of each rib is modeled with a uniaxial rotation joint. In the optimization, we introduce a constraint, which takes into account the fact that the adjacent ribs are connected by the intercostal muscle.

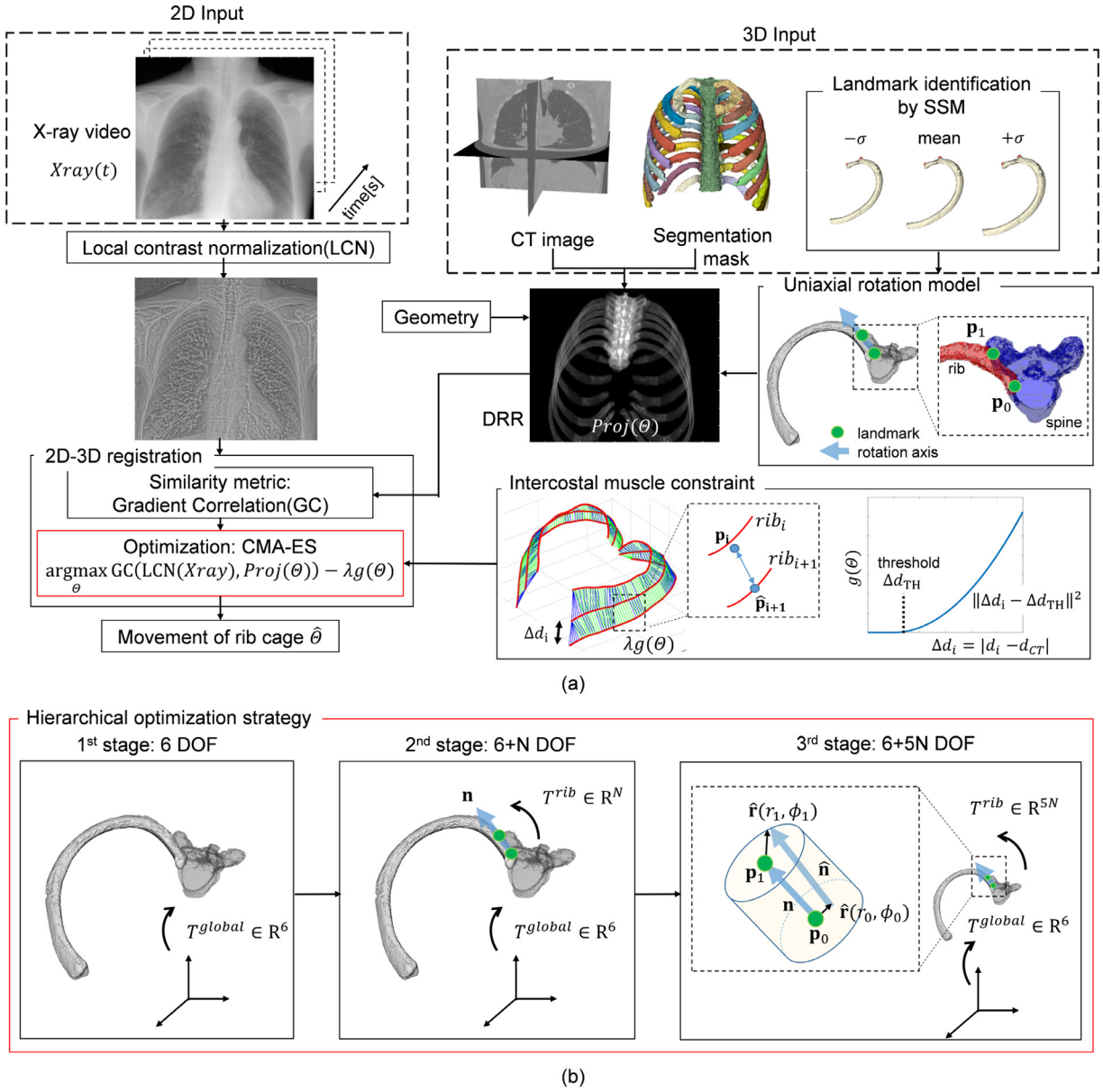

Fig. 1. (a) Workflow of the proposed method. The optimization parameter Θ represents the rigid transformation of the spine, and rotation axis and rotation angle of N ribs (note the rotation axis parameters are not optimized in the first stage). $g(\Theta)$ is a regularization term that penalizes the cost according to the distance between the ribs which acts like the intercostal muscles and facilitates a robust and anatomically feasible estimation. (b) Hierarchical optimization strategy in the proposed method. The first stage optimizes the global rigid transformation of the rib cage. The second stage jointly optimizes the local rigid transformation of the rib-rotation angle around the rotation axis **n** for each rib. The final stage jointly optimizes the rotation axis **n** within a small cylindrical region.

2.2. Preprocessing of CT

2.2.1. Segmentation of rib and spine in CT

We semi-automatically segment each rib bone and the spine in CT data using commercial interactive 3D-image-segmentation software, Synapse Vincent (Fujifilm, Tokyo, Japan). For the segmentation of the rib, we use the *bone separation module*, which requires the operator to select seed points interactively in each rib bone. For the segmentation of the spine, we used the *spine extraction module*, which allows us to extract spine semi-automatically. In our experiments, it took about 20 min for segmentation of the 2nd to 4th ribs and vertebrae of one case.

2.2.2. Estimation of rib landmarks using statistical shape model

The costotransverse and costovertebral joints on each rib, which define the initial estimate of the rotation axis, are automatically estimated using a statistical shape model (SSM). The workflow of the estimation process is illustrated in Fig. 2. The SSM of each rib, i.e., the average shape S_{ave} and variation modes, were computed using a method of SSM construction described in (Yokota et al., 2013) (but hierarchization was not adapted). Then, the anatomical landmarks, i.e., the costovertebral and costotransverse joints, manually identified on the average shape are automatically mapped on the target shape (L_T) by fitting the coefficients of the variation mode of the constructed SSM.

2.3. Preprocessing of radiography

Local contrast normalization is applied to the radiograph as a pre-process. It normalizes the intensity value within the neighborhood to zero mean and unit variance. Let x, y be vertical and horizontal indices of an interest pixel of input image $a \in \mathcal{R}^2$, and i, j

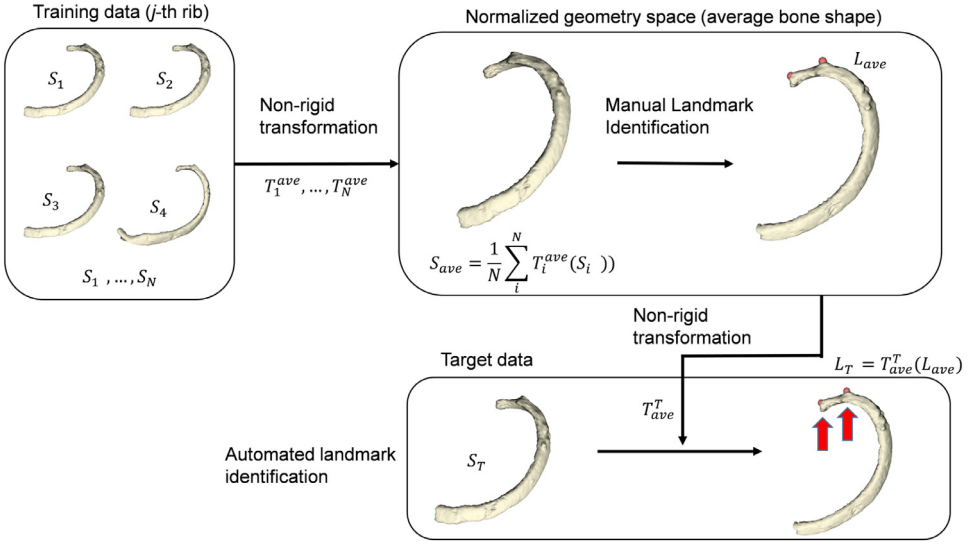

Fig. 2. Workflow of computing the anatomical landmarks on the rib bone. The landmarks are manually identified on the average bone shape (L_{ave}) and automatically mapped to the target shape (L_T) by statistical shape model (SSM) fitting.

be indices of the neighboring pixels. Now output image $\hat{a} \in \mathcal{R}^2$ is given by $\hat{a}_{xy} = \frac{\tilde{a}_{xy}}{\sigma_{xy}} = \frac{a_{xy} - \sum_{(i,j)} w_{ij} a_{i+x,j+y}}{\sqrt{\sum_{(i,j)} w_{ij} a_{i+x,j+y}^2}}$, where $\tilde{a}_{xy}$ and σ_{xy} are the average and standard deviation of the pixels within the neighborhood window, respectively. The weights w_{ij} are determined in such a way that their summation amounts to one ($\sum_{(i,j)} w_{ij} = 1$). In this study, all the weight values were uniform, i.e., all weights are $1/N$ where N is the number of pixels in the window, which is called the averaging filter. In the proposed method, LCN is used to enhance the contrast between the ribs and background soft-tissues such as the lungs and bronchia. In our experiments, the window size was empirically determined as 21 pixels. In the experiments using real images introduced in Section 3.2, we demonstrated how LCN improves the shape of the cost function and makes the optimization more robust.

2.4. Parameterization of rib motion

The rib cage consists of 12 pairs of ribs, which are connected to the thoracic vertebrae via joints. De Troyer et al. (2005) approximated rib motion using a uniaxial rotation about the axis connecting the costovertebral joint, which connects between the vertebral body and the head of rib, and the costotransverse joint, which connects between the transverse process and the tubercle of rib. The model was validated by Ito et al. (2011) by analyzing CTs at the inhale and exhale phases of one subject.

We formulate De Troyer's model as follows. Given the positions of the costovertebral joint ($\mathbf{p}_0$) and the costotransverse joint ($\mathbf{p}_1$) in the CT coordinate, the initial approximated rotation axis of the rib is defined by $\mathbf{n} = (\mathbf{p}_1 - \mathbf{p}_0)$. We denote a homogeneous transformation of the rib as matrix $rot(\mathbf{n}, \theta) \in \mathcal{R}^{4\times4}$, which represents a rotation θ around the axis $\mathbf{n}$. Note that the translation is not zero when line $\mathbf{n}$ does not pass through the origin. We parameterize $\mathbf{n}$ by using four parameters (r_0, ϕ_0, r_1, ϕ_1), as shown in Fig. 1(b) (see the caption for the definitions of the four parameters). The homogeneous transform T^{rib} with respect to the spine $T^{global} \in \mathcal{R}^{4\times4}$ is defined as

$$T^{rib}(\theta; r_0, \phi_0, r_1, \phi_1) = rot(\hat{\mathbf{n}}, \theta) \cdot T^{global}, \quad (1)$$

where,

$$\hat{\mathbf{n}} = \mathbf{n} + \hat{\mathbf{r}}(r_1, \phi_1) - \hat{\mathbf{r}}(r_0, \phi_0)$$
$$\hat{\mathbf{r}}(r, \phi) = r\{\cos\phi\ \mathbf{r} + \sin\phi(\mathbf{r} \times \mathbf{n})\}$$

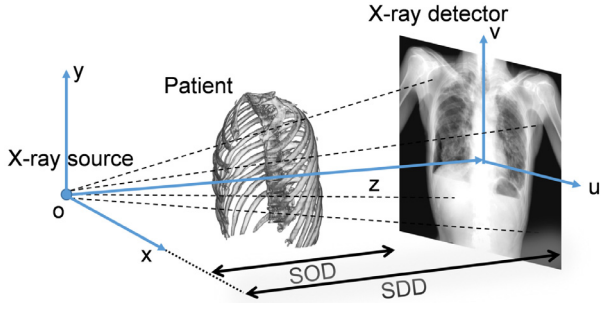

Fig. 3. Definition of projection geometry used in this study. Parameters associated with x-ray source and computed tomography (CT) and detector-coordinate systems are shown.

and $\mathbf{r}^T\mathbf{n} = 0$, and $|\mathbf{r}| = 1$. The T^{global} is represented with six parameters of translation and rotation (t_x, t_y, t_z, r_x, r_y, r_z). The ZYX Euler angle is used to describe rotation. We considered multiple vertebrae as one rigid object in this study. The rationale of this assumption is discussed in Section 4.

2.5. DRR generation

The DRR-based method, which is also called the intensity-based method, is known to be more accurate and robust than the feature-based method, where the image features such as contours or landmark points are first extracted and the distances between these features are minimized, because the intensity-based method does not rely on the error-prone segmentation of the features and utilizes all the information in the images (Markelj et al., 2012). The DRR is generated from a CT data using the ray-casting algorithm that computes line integrals of CT value along the passing ray.

In this paper, the x-ray imaging geometry is represented using the perspective projection model, as shown in Fig. 3. The origin of the detector-coordinate system is located at the center of the detector. The x and y axes are parallel to the detector coordinate, the z axis is parallel to their cross product, and the origin is at the position of the x-ray source. The location of the patient is (x, y, z) = (0,0, source-object distance (SOD)) and the distance from the x-ray source to the detector is denoted as the source-detector distance (SDD).

2.6. Similarity metric

The similarity metric used in the proposed 2D–3D registration method is gradient correlation (GC) (Penney et al., 1998). GC is the normalized cross correlation (NCC) between gradients of the source and target images, which is formulated as

$$\mathrm{GC}(A,B) = \frac{1}{2}\{\mathrm{NCC}(\nabla_x A, \nabla_x B) + \mathrm{NCC}(\nabla_y A, \nabla_y B)\} \tag{2}$$

where

$$\mathrm{NCC}(A,B) = \frac{\sum_{(i,j)}(A-\bar{A})(B-\bar{B})}{\sqrt{\sum_{(i,j)}(A-\bar{A})^2}\sqrt{\sum_{(i,j)}(B-\bar{B})^2}}$$

, the horizontal and vertical directions are denoted as Δ_x and Δ_y, and the source and target images are denoted as A and B, respectively.

2.7. Initialization of patient position

In our experiments, the geometric calibration of the imaging system was not carried out, and SOD and SDD were set to 1.8 and 2.0 m, respectively, which are approximate values used in a typical clinical protocol of chest radiography. Better geometric calibrations generally produce better registration results; however, obtaining an accurate calibration every time using a specially designed calibration phantom is difficult in a routine clinical setting. Through the experiments, we found that this simple assumption in the geometry still provided a reasonably accurate initialization of patient position, resulting in a robust registration. We further discuss the initialization in Section 4.

2.8. Regularization and optimization

To improve the robustness of optimization, we introduce the following penalized objective function that takes into account the effects of the intercostal muscle that connects the neighboring ribs and enforces the interlocking motion of the rib cage (i.e., the movement of each rib bone is not independent but is constrained by the relative position with respect to its neighboring ribs).

$$\hat{\Theta} = \arg\max_{\Theta} \mathrm{GC}(\mathrm{LCN}(Xray), Proj(\Theta)) - \lambda g(\Theta) \tag{3}$$

where

$$g(\Theta) = \begin{cases} \max_i (\Delta d_i - \Delta d_{TH})^2 & (\max_i(\Delta d_i) > \Delta d_{TH}) \\ 0 & (otherwise) \end{cases}$$

The term Θ denotes the parameters to optimize, which represent the transformation of all the rib bones, $Proj(\Theta)$ is the simulated projection image (i.e., DRR) of the rib bones whose positions are parameterized by Θ, $LCN(Xray)$ represents the actual x-ray image after the LCN pre-process, and $g(\Theta)$ is the regularization term that penalizes the objective function according to the distance between the neighboring ribs. The distance between the ith rib and its neighboring rib in a reference-phase CT (maximum exhale phase in our experiments) is defined as Δd_i, which we compute as

$$\Delta d_i = \frac{1}{|p_i|}\sum_{\mathbf{p}_i \in p_i} \left\{ \|T^{rib,i}\mathbf{p}_i - T^{rib,i+1}\hat{\mathbf{p}}_{i+1}\| - \|\mathbf{p}_i - \hat{\mathbf{p}}_{i+1}\| \right\}$$

where

$$\hat{\mathbf{p}}_{i+1} = \arg\min_{\mathbf{p}_{i+1} \in p_{i+1}} \|\mathbf{p}_i - \mathbf{p}_{i+1}\|$$

The term $\mathbf{p}_i$ is a point set representing the center line of the ith rib bone computed from its segmentation mask using the skeletonization algorithm based on the distance field and fast matching method (Van Uitert and Bitter, 2007).

By enforcing the constraint on the distance between adjacent ribs so that it does not largely deviate from its initial distance, the penalty term helps maintain the anatomically plausible rib-cage shape, preventing mis-registration by incorrectly matching one rib in the CT to the other ribs in the projection image. The parameter λ is a weight used to balance the similarity-metric term and the penalty term. In this study, λ and Δd_{TH} were empirically determined as 1×10^{-4} and 5 mm, respectively.

A stochastic optimization algorithm called covariance matrix adaptation evolution strategy (CMA-ES) (Hansen, 2006) is used for optimization. This highly parallelizable evolution strategy is especially beneficial on GPU implementation, as detailed in a previous study (Otake et al., 2012). The proposed optimization strategy consists of three stages. The first stage optimizes the global rigid transformation of the rib cage (6 DoFs for a rigid object consisting of all vertebrae and ribs). The second stage uses the result of the first stage as an initial estimate to jointly optimize the local rigid transformation of the rib-rotation angle θ around the rotation axis $\mathbf{n}$ for each rib ($6+N$ DoF for N ribs) assuming the relative position of the rotation axis with respect to the vertebrae is fixed. The final stage uses the result of the second stage as an initial estimate to further jointly optimize the rotation axis $\mathbf{n}$ within a small cylindrical region (i.e., $\mathbf{n}$ is perturbed inside the cylinder with radii of r_0 and r_1 at its base, as shown in Fig. 1(b)). The two-level multi-resolution pyramid (Otake et al., 2013) was used in each stage to improve robustness against local optima. The optimization parameters used in our experiments are summarized in Table 1.

2.9. Error metric and ground truth

One of the common error metrics used in evaluating 2D–3D registration is the mean projection distance (mPD) (van de Kraats et al., 2005), which is the average distance in the projection plane between anatomical landmarks defined on the target bone in 3D (and projected onto the 2D plane with the computed transformation) and its corresponding ground truth point in the 2D x-ray image. The mPD metric requires identification of the corresponding anatomical landmarks in the x-ray image, which is quite difficult and error-prone in the case of rib bones because of their smooth surfaces with a small number of feature points. Therefore, in this study, we evaluated the error using the contour lines in the projection plane similar to a previous study (Lamecker et al., 2006), which we call the mean projected contour distance (mPCD). Given the true contour s_i of an ith rib projected onto the x-ray image and a contour s_i' in the DRR of a rib at an estimated pose, mPCD is computed as

$$\mathrm{mPCD} = \frac{1}{|s_i|}\sum_{\mathbf{x}\in s_i} \min_{\mathbf{x}' \in s_i'} \|\mathbf{x} - \mathbf{x}'\|^2. \tag{4}$$

Example registration results with different mPCD values are illustrated in Fig. 4. The ground truth in the real-image experiments was defined manually by tracing the contours of the rib in the x-ray images.

3. Results

3.1. Simulation experiments

In the simulation experiments, we used DRRs of the two-time-phase CTs, acquired at maximum inhale and maximum exhale phases, included in the EMPIRE10 data set (Murphy et al., 2011) as the target image. The detailed specifications of the data set are listed in Table 2. Among 30 cases in the EMPIRE10 data set, we selected 6 that include both maximum inhale and maximum exhale phases, as shown in Fig. 5. Fig. 5 also illustrates the rotation angle of each rib between the two phases, which was computed by

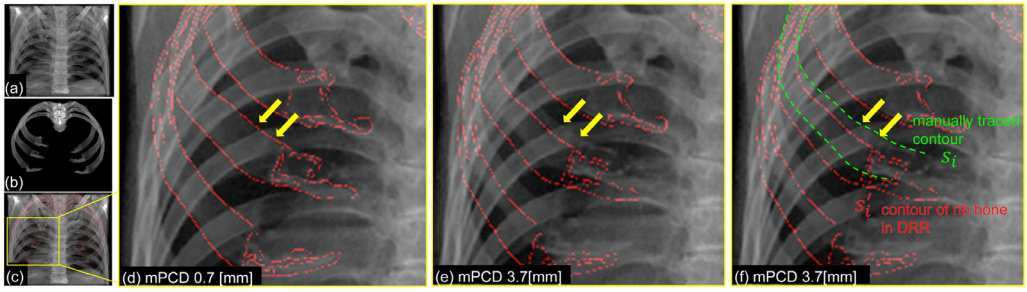

Fig. 4. Error metric used in this study, mean projected contour distance (mPCD), and example registration results with different mPCD values. (a) X-ray image, (b) digitally reconstructed radiograph (DRR) at the estimated pose, (c) overlaid with the DRR edges (in red), (d)(e) enlarged view of the trials with different mPCD values. The yellow arrows indicate the true contour of the rib on the x-ray image. The result with mPCD of 0.7 mm (d) exhibits almost no visually recognizable difference between the lines while 3.7 mm (e) shows a clear discrepancy. (f) mPCD was defined as the distance between the manually traced contour (green dashed line) of each rib bone on the x-ray image and the automatically detected contour on the DRR (red dashed line). (For interpretation of the references to color in this figure legend, the reader is referred to the web version of this article).

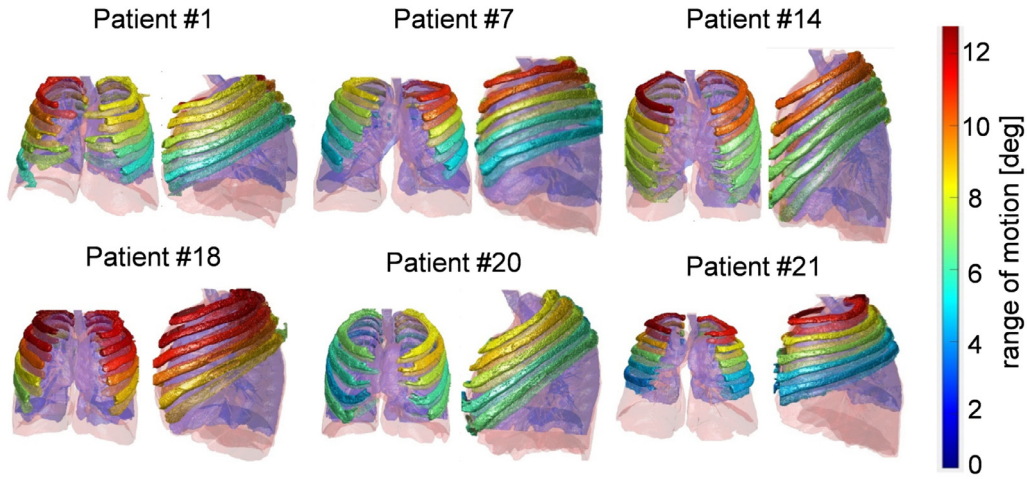

Fig. 5. Rib cage and lungs of six cases in EMPIRE10 data set that were used in the evaluation experiments. CT images at inhale and exhale phases were analyzed. Color of each rib indicates the rotation angle between inhale and exhale phases (see the colormap on the right). The opaque and transparent ribs show the inhale and exhale phases, respectively (they overlap each other in some cases). The lungs at inhale and exhale phases are shown in red and blue. The larger rotation angle was observed at the ribs of the superior levels. (For interpretation of the references to color in this figure legend, the reader is referred to the web version of this article).

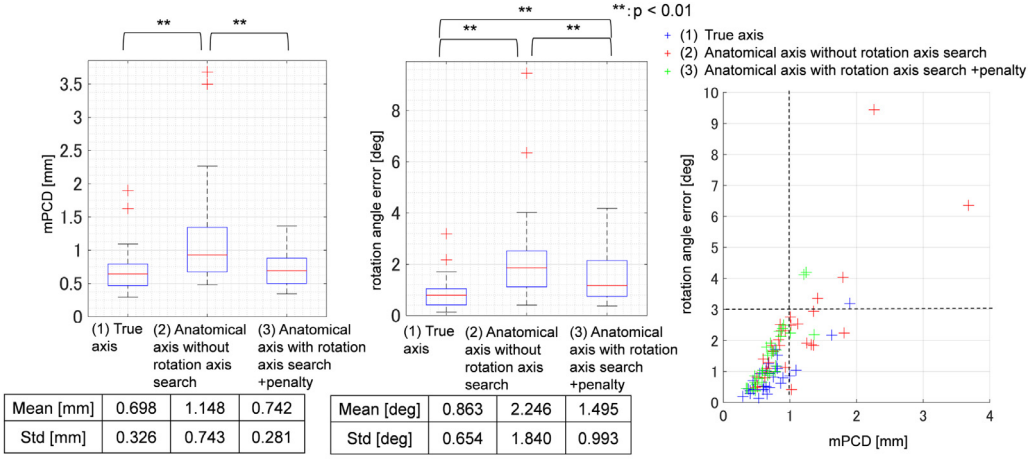

	(1) True axis	(2) Anatomical axis without rotation axis search	(3) Anatomical axis with rotation axis search +penalty
Mean [mm]	0.698	1.148	0.742
Std [mm]	0.326	0.743	0.281

	(1) True axis	(2) Anatomical axis without rotation axis search	(3) Anatomical axis with rotation axis search +penalty
Mean [deg]	0.863	2.246	1.495
Std [deg]	0.654	1.840	0.993

Fig. 6. Results of simulation experiments. (a-b) box and whisker plots for different search scenarios. (a) is used mPCD and (b) is used rotation-angle error as error metric. Boxes denote the 1st/3rd quartiles, the median is marked with the horizontal line within each box, and outliers are marked with crosses. (c) The scatter plot showing the rotation angle error as a function of mPCD. The correlation between the two metrics suggested validity of using mPCD, the error metric observable in the projection image, as an indicator of the unobservable 3D rotation-angle error.

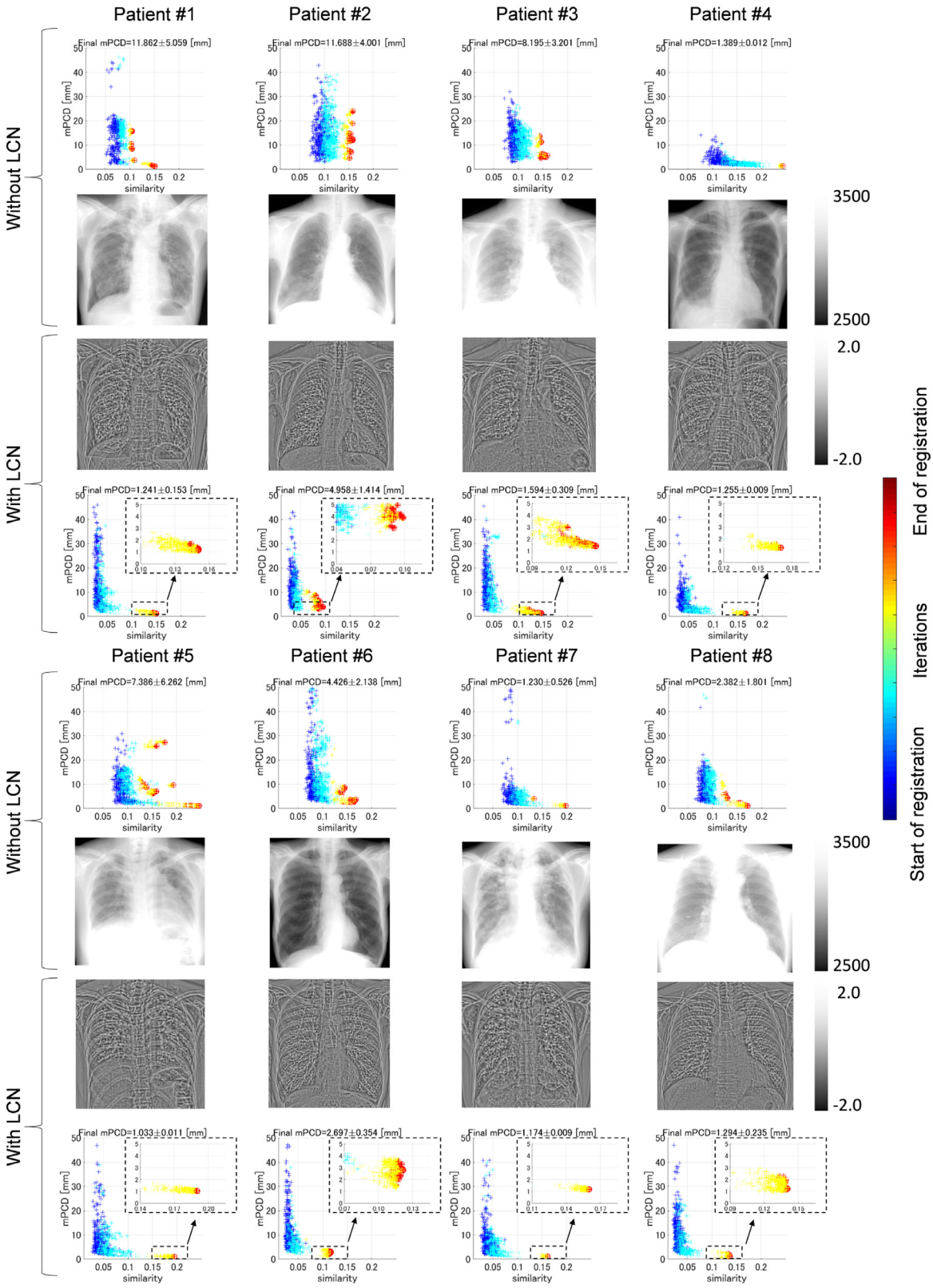

Fig. 7. Analysis of similarity metric *landscape* to investigate the effectiveness of local contrast normalization (LCN). The mPCD is plotted as a function of the similarity measure (GC) in the top and bottom rows of each patient. The color of each cross indicates the progression of iterations in the optimization process (i.e., the registration started from the blue cross and converged at the red cross). Thirty optimization trials were carried out for the first frame of each patient. One cross represents an average over 100 function evaluations (approximately 5×10^4 function evaluations were conducted in one trial). The red circle indicates the converged solution. Note that the red crosses in the bottom row (with LCN) are more concentrated and show lower mPCD than the top row (without LCN), indicating that LCN improved both robustness and accuracy. (For interpretation of the references to color in this figure legend, the reader is referred to the web version of this article).

Table 1
Summary of optimization parameters.

Optimization stage		First stage: Global transformation search	Second stage: Rib angle search	Final stage: Rib axis search
Dimension of solution space		6	6+N	6+5N
Population size (1st-level, 2nd-level in Gaussian resolution pyramid)		(200, 100)	(200, 100)	(200, 100)
Number of multi-starts		30	10	10
Regularization	Lambda	–	1×10^{-4}	1×10^{-4}
	Δd_{TH} [mm]	–	5	5
Upper/lower bound of search space	Translation (x, y, z) [mm]	(± 50, ± 100, ± 150)	(± 50, ± 50, ± 50)	(± 10, ± 10, ± 10)
	Rotation (x, y, z) [°]	(± 15, ± 15, ± 15)	(± 15, ± 15, ± 15)	(± 5, ± 5, ± 5)
	Rib angle [°]	–	± 15	± 5
	Rib axis (r, ϕ) [mm, °]	–	–	(± 15, ± 180)

Table 2
Specification of data set used in experiments.

Simulation experiments (8 cases included in EMPIRE10)		
CT (source)	Dimension (avg.)	$438 \times 329 \times 399$ [pixel]
	Pixel spacing	0.63–0.77 [mm]
	Slice spacing	0.7 [mm]
	Breathing phase	Exhalation
DRR (target)	Dimension	1344×1344 [pixel]
	Pixel spacing	0.32×0.32 [mm]
	Breath phase	Inhalation
Real image experiments (8 cases)		
CT (source)	Dimension (avg.)	$512 \times 512 \times 120$ [pixel]
	Pixel spacing	0.68×0.68 [mm]
	Slice spacing	2.5 [mm]
	Posture	Supine
	Breathing phase	Exhalation
X-ray video (target)	Dimension	1344×1344 [pixel]
	Pixel spacing	0.32×0.32 [mm]
	Number of frames	36
	Frame rate	3 [fps]
	Posture	Standing

applying the 3D–3D surface registration, the iterative closest point (ICP) algorithm (Besl et al., 1992), on the rib surfaces that were segmented from the CTs. Note that there were no recognizable deformations of spine curvature between the two time-phases because the subject stayed in the supine position during both scans. Therefore, the experimental setup was suitable for evaluating the effectiveness of the proposed rib-motion model excluding one potential error factor, which is spine deformation. To simulate the quantum noise appearing in real x-ray images, the Poisson random noise computed based on the exposure level at a uniform 1.985×10^5 photons per detector element for an un-attenuated beam was applied to the target DRR (Prince and Links, 2014). Note that the photon counts were computed from the un-attenuated beam in the real x-ray image acquired with our clinical protocol, which is explained in detail in the next section.

In the proposed method, we estimate the rotation axis as well as the rotation angle of the ribs. Thus, in the following explanation of our experiments, we use the term *true rotation axis* to compare the registration accuracy with an ideal situation in which the rotation axis is accurately known. The *true rotation axis* was computed via ICP registration as explained above. We denote the translation and rotation from the exhale phase to the inhale phase as t_{GT} and R_{GT}, respectively, and the translation to the *true rotation axis* as t_C. The rotation matrix R_GT is represented as the axis-angle representation based on the Rodrigues' rotation formula, and the axis vector was used as the direction of the *true rotation axis*.

The evaluation of the proposed uniaxial joint model and rotation-axis search was conducted by comparing the registration error in the following three scenarios. (1) Angle search with the true axis using two-time-phase CT: Optimization of the rotation angle using the *true rotation axis* (i.e., the simplest case in which one DoF rotation around the axis provides the registration that perfectly matches the rib bone in the two phases). (2) Angle search using a single-time-phase CT: Optimization of the rotation angle using the axes defined by the anatomical landmarks, which we call *anatomical axis* (i.e., the simple one-DoF optimization with a realistic scenario in the case in which we have only single-time-phase CT and the *true rotation axis* is not available). (3) Angle+axis search using a single-time-phase CT (proposed method): Optimization of one rotation angle and four rotation-axis parameters representing its direction using the *anatomical axis* as an initial estimate (i.e., a method in which the optimization is most involved though accurate).

The results of the simulation experiments with six ribs (2nd, 3rd and 4th ribs on the left and right sides) of six patients are shown in Fig. 6 (i.e., $n = 36$ data points in total). Since the CMA-ES produces different optimization results even with the same initialization due to the stochasticity in generation of the population, 20 trials from the same initialization were carried out and their average is shown in the figure. Scenario (3), the proposed method with rotation-axis search, provided statistically significant improvement (double asterisk (**) indicates that the p-value was less than 0.01) by the Welch's test in mPCD (mean $\pm$ std: 0.742 ± 0.281 mm) and the rotation angle error ($1.495 \pm 0.993°$) compared to scenario (2), which is the angle search with the *anatomical axis*. The error is not supposed to be zero even with the *true rotation axis*, i.e., scenario (1), because of the following two reasons: effect of soft tissues and the axis estimation error. The main potential error source is the soft tissues in the simulated image that was introduced to enhance the realism of the experiment. The soft tissues created false local optima, causing the degradation of the accuracy. Moreover, what we call the *true rotation axis* might have error due to the error in ICP registration of the two-time-phase CT.

The scatter plot in Fig. 6(c) shows the relationship between mPCD (the error metric in 2D projection) and the rotation-angle error (the error metric in 3D space). All registration trials with an mPCD value smaller than 1.0 mm (left side of the vertical dotted line) were with the rotation-angle error smaller than 3.0° (lower side of the horizontal dotted line), suggesting the effectiveness of mPCD, which is observable in the 2D projection image, as an error metric to detect registration failure.

Moreover, in order to evaluate the effectiveness of the proposed uniaxial joint model, we conducted the registration with non-uniaxial joints, resulting in a rotation-angle error of $11.139 \pm 4.124°$ and mPCD of 5.844 ± 2.433 mm. The overall result in the simulation experiments is shown in Table 3.

To evaluate the influence of the Poisson random noise in the simulation experiments, we evaluated the registration accuracy without the noise using the *true rotation axis* and found a

Table 3
Results of the simulation experiments. The mean and standard deviation of mPCD and rotation angle error are reported for each scenario. For the statistical significance, refer to Fig. 6.

mPCD [mm]				
	Non-uniaxial model	Uniaxial model		
		True axis	Anatomical axis	
			w/o rotation axis search	w/ rotation axis search
w/o penalty	5.844 ± 2.433	0.698 ± 0.326	1.148 ± 0.743	0.757 ± 0.288
w/ penalty	5.355 ± 2.043	0.664 ± 0.284	1.151 ± 0.736	0.742 ± 0.281
Rotation angle error [°]				
	Non-uniaxial model	Uniaxial model		
		True axis	Anatomical axis	
			w/o rotation axis search	w/ rotation axis search
w/o penalty	11.139 ± 4.124	0.863 ± 0.654	2.246 ± 1.839	1.539 ± 0.993
w/ penalty	10.161 ± 3.454	0.840 ± 0.686	2.237 ± 1.808	1.495 ± 0.993

slight accuracy improvement (0.664 ± 0.284 mm, $0.840 \pm 0.686°$ to 0.661 ± 0.300 mm, $0.818 \pm 0.693°$, for mPCD and rotation-angle error, respectively).

These results indicate the effectiveness of the rib-motion model constrained by a uniaxial joint as well as the importance of accurate estimation of the rotation axis. The highest accuracy was achieved when the *true rotation axis* computed from the two-time-phase CT was used. The rotation-angle error significantly increased in the scenario using the *anatomical axis*, which has been regarded as the rotation axis of ribs since De Troyer's model (De Troyer et al., 2005) was introduced, while the error decreased to the level close to that with the *true rotation axis* when the rotation axis was jointly searched along with the rotation angle of the ribs in the optimization. In practice, the *true rotation axis* is only available when we acquire a two-time-phase CT, which requires higher radiation dose. The proposed rotation-axis-search approach with a rough initial estimate by De Troyer's anatomical landmarks can be considered as a practical alternative in routine clinical practice or annual screening examinations in which a lower-dose modality is preferable. Note that, in this study, we automatically obtained the initial estimate of the axis from an individual single-time-phase CT using a statistical modeling of the anatomical landmarks.

3.2. Real-image experiments

In the real-image experiments, we used x-ray videos acquired when the patients were in standing position while breathing and CTs of each patient acquired in the supine position at the inhale phase of eight cases, as detailed in Table 2. The study protocol was approved by our institutional review board (#598-1 at Kanazawa University, Japan). Each x-ray video consisted of 30 frames acquired over one breathing cycle in 10 s starting from the maximum exhale phase. The entrance-surface dose for the 30 frames, measured in air without backscattering, was approximately 0.4 mGy, which was less than that in the lateral chest radiography with the protocol suggested by the International Atomic Energy Agency (IAEA), which is 1.5 mGy (Tanaka et al., 2015). The experiments with the real images allowed us to analyze the robustness of the proposed method against the properties in a real x-ray-imaging device that were not considered in the simulation experiments, yet might adversely affect registration accuracy, such as the polyenergetic x-ray spectrum, x-ray scatter, and finite focal spot size. Note that the slice spacing of the CT used in our clinical protocol was larger than that of the EMPIRE10 data set used in the simulation experiments. We applied the spline interpolation in the out-of-plane direction and created a volume with 0.625 mm slice spacing before the pre-process to suppress the aliasing effect appearing in the DRR.

For quantitative evaluation of the registration accuracy, four frames at 2.5 s intervals were selected for each patient, and the true contour of each rib was manually traced to calculate mPCD. As is the case with any real patient studies, the ground truth data of the actual rib-rotation angle in the 3D space were not available. Therefore, we assessed the registration accuracy by the contour error appearing in the 2D projection plane, which our simulation experiments suggested to be correlated with the 3D rib-rotation angle.

First, we investigated the effect of LCN on the cost function and on robustness of the 2D-3D registration with real x-ray images acquired with the low-dose protocol. The comparison of the results with and without LCN is shown in Fig. 7. The scatter plots show mPCD as a function of the similarity measure, GC, of 30 trials of the 6 ribs for each patient.

In the analysis of numerical optimization, the goodness of the cost function was generally measured with the shape of the plot of the cost value as a function of the optimization parameters, which is often called the *landscape* (Talbi, 2009). In particular, the dispersion metric (Lunacek and Whitley, 2006) was proposed to quantitatively determine whether the local optima in the cost function are dispersed over the parameter domain or rather concentrated at one point. The cost function with concentrated local optima is considered better for optimization than that with dispersed local optima. Our analysis illustrated in Fig. 7 is based on a similar idea, though we used the error metric (i.e., mPCD) as the x-axis rather than the optimization parameter to verify the validity of our similarity metric as well as the dispersion of local optima. In the registration problem, the global optimum of the cost function does not necessarily yield the minimum error in cases, for example, (1) the choice of similarity metric is not appropriate and (2) there is a mismatch between the image-simulation process (i.e., DRR generation in our case) and the actual image-acquisition process. As shown in Fig. 7, we first confirmed that the global maximum of the similarity metric actually yielded the minimum mPCD, suggesting that the effect of (1) and (2) mentioned above is reasonably small and the similarity metric we used worked as intended. We define the shape of the function that relates the similarity to error metric as similarity metric *landscape*, following customary expressions in the field of mathematical optimization. The *landscape* allows an intuitive analysis of suitability of the similarity metric for the target registration problem. We then observed that the similarity metric *landscape* with LCN is clearly better than that without LCN, showing a smaller number of local optima concentrated to the smallest mPCD value. The mean and standard deviation of the final mPCD

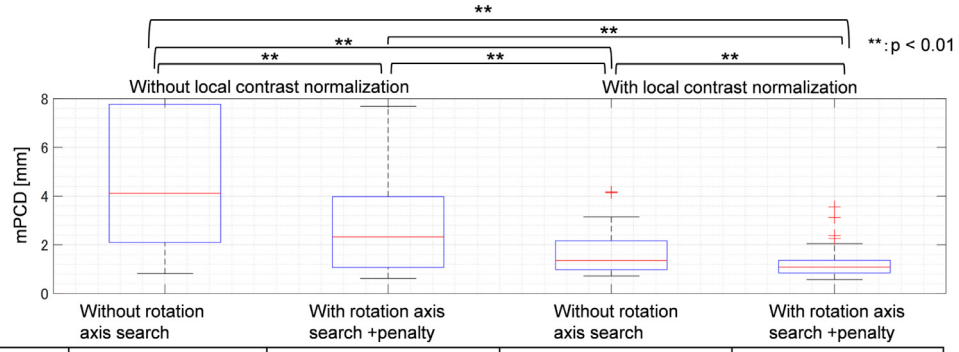

Mean [mm]	6.358	2.607	1.628	1.255
Std [mm]	6.636	1.798	0.851	0.615

Fig. 8. Quantitative evaluation results of the real-image experiments with 6 ribs (2nd, 3rd and 4th ribs of both sides) of 8 patients (i.e., 48 data points in total). The mean and standard deviation for each scenario are listed in the table below. The error was significantly decreased by adding the rotation axis search and penalty term, and further decreased by adding the preprocessing with LCN.

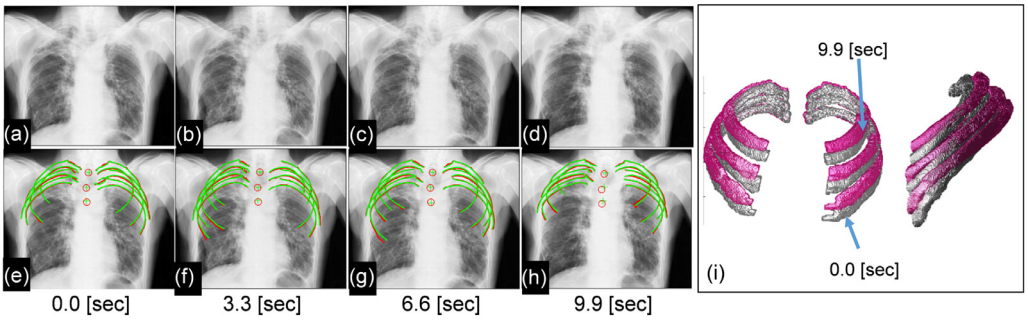

Fig. 9. Visualization of the registration results at 4 representative frames of patient #1 in the real image experiment. (a-d) The original x-ray image, (e-h) overlaid with the contours of the ribs (green: manually identified ground truth, red: estimated) and the center of vertebrae (green cross: ground truth, red circle: estimated). (For interpretation of the references to color in this figure legend, the reader is referred to the web version of this article).

values also clearly improved with LCN. Also note that in the case of patient #4, in which the image contrast over the entire image was rather uniform resulting in a relatively clear boundary of the rib bones even without LCN, the *landscape* looks better than the other cases. This indicates that LCN correctly worked for the cases in which the contrast was not uniform in the original x-ray image and the similarity metric was not useful to stably find the correct alignment due to the confusing edges around the true rib region.

Finally, quantitative evaluation of LCN and the rotation-axis search were conducted by comparing the registration error for the four scenarios: With/without LCN and the rotation-axis search. The results with six ribs of eight patients are shown in Fig. 8 (i.e., $n = 48$ data points in total). The average of the four frames is shown in the plot. The case with both LCN and rotation-axis search yielded statistically significant improvement of Welch's test ($p < 0.01$) in mPCD (1.255 ± 0.615 mm) compared with all other cases.

Table 4 shows the overall result in the real-image experiments. mPCD was improved from 1.548 ± 0.810 mm to 1.255 ± 0.615 mm in these experiments.

In order to evaluate the sensitivity of LCN to the window size, registration accuracy was evaluated with window size of 11, 21, and 31, all of which provided a visually reasonable filtered image. The error with the rotation axis search with penalty (i.e., the proposed method) was 1.280 ± 0.627 mm, 1.255 ± 0.615 mm, and 1.272 ± 0.662 mm, respectively, which suggested robustness against the window size.

Although the proposed method improved robustness significantly, we still observed failures, which can be classified into two major modes: failures (1) due to insufficient contrast-to-noise ratio in the image even after LCN and (2) due to an irregular joint rotation that does not fit to our uniaxial motion model. Patient #2 had a low contrast-to-noise ratio; thus the gradient image was noisy, which created many false local optima in the cost-function space and led to failures (mPCD $>$ 4 mm) in some trials. In case of patient #6, the final registration error was larger than others (mPCD $>$ 2.5 mm) though the spine was aligned correctly based on visual verification, which may suggest that the rib motion did not follow the assumption of the uniaxial joint model. Even for those two patients (#2 and #6) that did not result in a clinically acceptable accuracy, Fig. 7 suggests a considerable improvement in robustness by applying LCN.

Fig. 9 shows an example visualization of the registration results in the real-image experiment. The manually traced contour (lines in green) and estimated contour (red) are overlaid to visually confirm the registration accuracy. Fig. 10 shows the 3D visualization

Table 4
Results of the real-image experiments. The mean and standard deviation of mPCD are reported for each scenario. For the statistical significance, refer to Fig. 8.

mPCD [mm]			
		Uniaxial model with anatomical axis	
		w/o rotation axis search	w/ rotation axis search
w/o LCN	w/o penalty	6.358 ± 6.636	6.436 ± 6.998
	w/ penalty	2.708 ± 1.815	2.607 ± 1.798
w/ LCN	w/o penalty	1.628 ± 0.851	1.548 ± 0.810
	w/ penalty	1.392 ± 0.711	1.255 ± 0.615

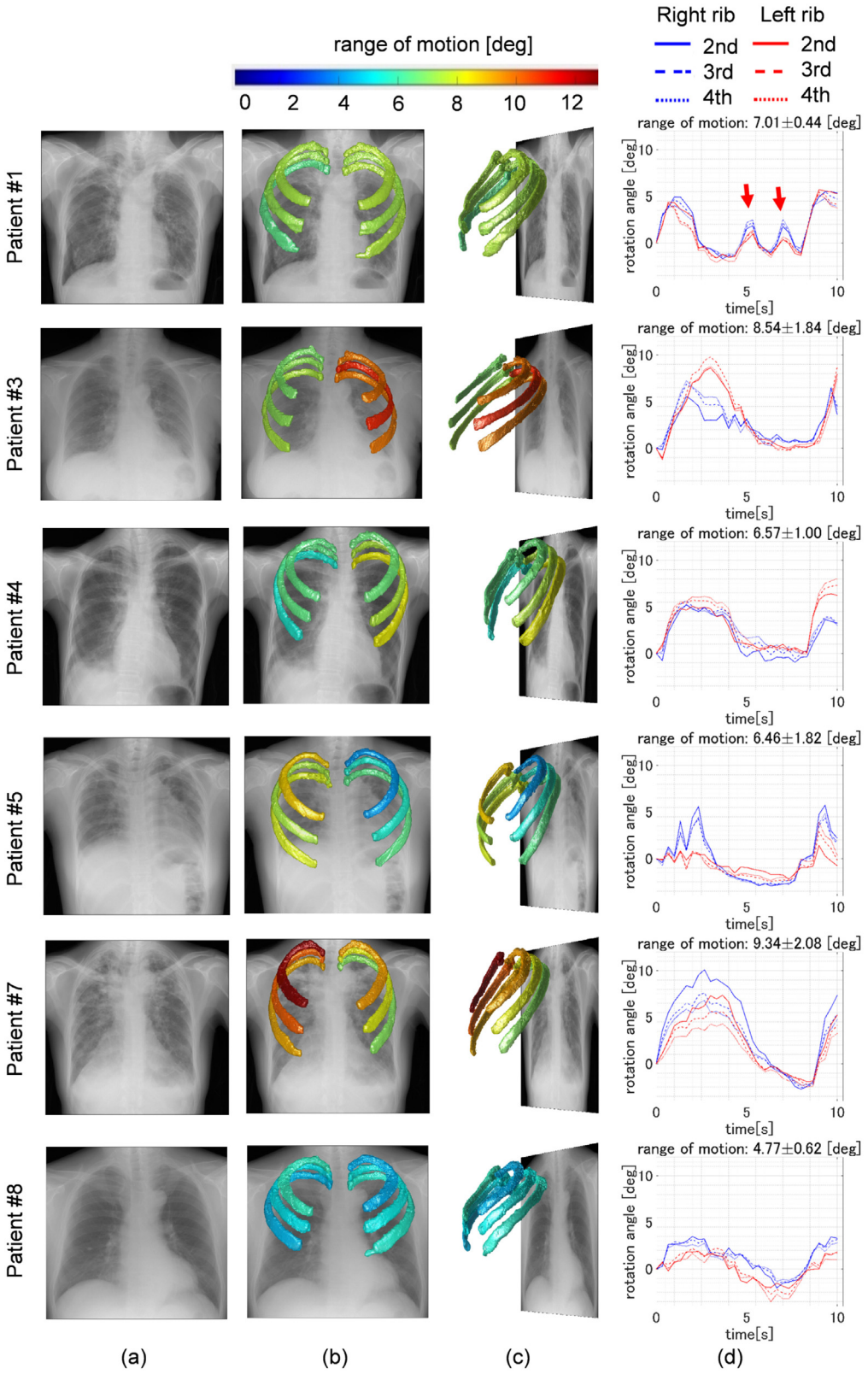

Fig. 10. Visualization of the registration result of all cases in the real image experiment. (a) The original x-ray image, (b,c) overlaid with the 3D rib model at the estimated pose. The color of each rib indicates the range of motion, which is defined as the difference between the maximum and minimum rotation angle in the ten seconds acquired by the video. The color difference between right and left ribs in patient #5 indicate left-right asymmetry motion. (d) The rib rotation angle around the rotation axis as a function of time. The 2nd, 3rd and 4th ribs of right and left sides were plotted for each patient. The reference of the rotation angle (0°) was the rotation angle estimated at the first frame of the x-ray video. The blue and red lines shows the ribs of right and left sides, respectively. (For interpretation of the references to color in this figure legend, the reader is referred to the web version of this article).

of the reconstructed motion color-coded by the range of motion of each rib, similar to Fig. 5, though the colors in Fig. 10 were computed from a single-time-phase CT and an x-ray video while those in Fig. 5 were from a two-time-phase CT. In this paper, we define the range of motion as the difference between the maximum and minimum rib-rotation angles within the 10 s in the video. The plots in Fig. 10(d) show the motion pattern of the 2nd to 4th ribs as a function of time for one breathing cycle. Based on the error analysis in the simulation experiments, which is $1.495 \pm 0.993°$ with the rotation-angle search, and the range of motion, $7.115 \pm 2.018°$, the proposed method would provide a reasonable estimate of the trend in the motion that is associated with a clinically important symptom of diseases such as the left-right asymmetric motion in patient #5 and the abrupt swing of the ribs that deviates from the normal breathing cycle indicated with the red arrows in patient #1 of Fig. 10(d).

The proposed method was implemented on MATLAB ver. R2015b (MathWorks, Natick, MA), which included function calls for rendering DRRs and computing the similarity metric on the GPU with CUDA 8.0 (nVidia, Santa Clara, CA). The average number of function evaluations, including DRR rendering and computation of similarity measure, conducted in one registration trial and the total computation time were approximately 5×10^4 and 5 min without the rotation-axis search and 2×10^5 and 20 min with rotation-axis search. Note that the real-time application is not our main focus in this paper. Although previous work such as (Gendrin et al., 2012) used a non-evolution strategy for optimization and demonstrated faster computation time than our current study, the evolution strategy such as CMA-ES provides a much higher robustness as shown in (Gill et al., 2012; Otake et al., 2013) at the sacrifice of longer computation time due to a large number of evaluation of cost function in each generation. In this study, our focus is robustness against local-minima rather than computation time, thus we selected CMA-ES.

4. Discussion

4.1. Effectiveness of the proposed method

One of the advantages of the analysis using the x-ray video over another approach that acquires multiple-phase CTs, for example so-called 4D CT, is significant reduction in radiation exposure. In a clinical scenario in which periodical follow-up screening examinations are required, the difference in radiation exposure is even larger since the proposed method requires only one CT image at the first examination and can use it with lower-dose x-ray videos in repetitive examinations as long as the shape of the bones remains unchanged.

We evaluated the proposed method through simulation experiments using the two-time-phase CT (i.e., inhale and exhale phases) and real-image experiments using x-ray videos acquired with a protocol used in a routine clinical setting. In both simulation and real-image experiments, the optimization of the rotation axis yielded statistically significant improvement ($p < 0.01$) compared to the scenario without rotation-axis search. A uniaxial rib-motion model together with the optimization of the rotation axis to improve robustness in optimization while maintaining a high degree of accuracy. We also confirmed the effectiveness of LCN in the real-image experiments. The LCN in the pre-processing of x-ray video to better condition the cost function space.

In this study, for the first time to the best of our knowledge, we demonstrated that LCN actually changed the cost-function space in a way that is suitable for optimization, as clearly shown in Fig. 7.

4.2. Application to other tasks

Initialization of registrations is a critical aspect that affects on success of registration. The x-ray videos we used in this study were obtained in a standard clinical protocol of standing chest x-ray using a fixed source and detector. Therefore, we initialized the registration using the prior knowledge about the position of the patient relative to the detector (i.e., SDD = 2.0 m, SOD = 1.8 m) and found that this simple initialization without using an accurate geometric calibration resulted in a reasonably high success rate and low registration error in the real image experiments. However, Villard et al. (2014) described the potential use of 2D–3D registration of the ribs in an intraoperative navigation using images acquired from a mobile x-ray C-arm for estimating liver deformation co-occurring with rib motion. In such an application scenario, the patient position relative to the detector is different from our setup. An application-specific initialization considering the setup of each imaging device would be necessary. The setup is generally consistent in a specific type of surgery and a simple assumption similar to the one we used in this study may be applied to other setups.

4.3. Limitations

One limitation of this study was the lack of evaluation with patients with scoliotic spines. In scoliotic patients, the rotation axis of the ribs significantly differs from healthy subjects, or the movement may not follow the uniaxial joint model. Further clinical evaluations are needed to assess the clinical applicability of the proposed method. A more sophisticated motion model considering the scoliosis in such patients is also necessary.

Another potential limitation is lack of deformation of vertebrae in the model. As described in Section 2.4, we considered our target vertebrae (T2–T4) as one rigid object. One potential rationale for this assumption came from the study by Beillas et al. (2009), in which they investigated the relationship between the body posture and spine curvature in nine subjects using an MRI scanner (Fonar Upright, Melville, NY) that allows acquisition in both standing and supine positions. They found that the difference in the T4–T12 thoracic kyphosis angle (i.e., forward rounding curve of the thoracic vertebrae) between standing and supine positions was $16 \pm 4°$. Assuming that the spine is curved at a regular interval at each intervertebral disc, the kyphosis angle per disc is 2.3°. Therefore, in this study, we considered that the change in the curvature from T2 to T4 is small enough to be modeled as one rigid object. However, we acknowledge that further investigation of the effect of this assumption in diseased patients is necessary. A more sophisticated spine model such as the statistical shape and pose model proposed by Rasoulian et al. (2013), may be incorporated to improve registration accuracy.

In proposed method, segmentation of each rib bone is required manual interaction (i.e., seed placements for each rib). One possible method to automate the segmentation would be to use a machine learning approach.

4.4. Future work

Our future work includes incorporation of the knowledge on temporal continuity as the regularization method similar to that proposed by Chen et al. (2013). By imposing the temporal continuity constraint in the optimization of time-sequential frames, a smoother motion, which is generally more plausible in terms of physical principle, can be obtained, although it sacrifices detectability of abrupt motion which is critical in the diagnosis of certain diseases. This trade-off requires investigation. Another future work is automated detection of registration failure, which

would reduce human interaction and potentially improve robustness by repeating the registration trial from a different initialization in case of failure. We plan to apply a convolutional neural network (CNN) to failure detection. A CNN would be able to be trained to predict the error metric in the projection plane, mPCD, directly from the registration results.

5. Conclusion

We proposed a robust 2D-3D registration method for 3D rib-motion recovery from dynamic radiography. Specifically, the contributions of this paper are the introduction of (1) a uniaxial rib-motion model together with the optimization of the rotation axis to improve robustness in optimization while maintaining a high degree of accuracy, and (2) the LCN in the pre-processing of x-ray video to better condition the cost function space. We evaluated the proposed method through simulation experiments using the two-time-phase CT (i.e., inhale and exhale phases) and real-image experiments using x-ray videos acquired with a protocol used in a routine clinical setting. In both simulation and real-image experiments, the optimization of the rotation axis yielded statistically significant improvement ($p < 0.01$) compared to the scenario without rotation-axis search. We also confirmed the effectiveness of LCN in the real-image experiments.

Acknowledgements

This research was supported by MEXT/JSPS KAKENHI 26108004 and JST PRESTO20407.

Supplementary material

Supplementary material associated with this article can be found, in the online version, at doi:10.1016/j.media.2018.10.002.

References

Beillas, P., Lafon, Y., Smith, F.W., 2009. The effects of posture and subject-to-subject variations on the position, shape and volume of abdominal and thoracic organs. Stapp Car Crash J. 53, 127.

Besl, P.J., McKay, N.D., et al., 1992. A method for registration of 3-d shapes. IEEE Trans. Pattern Anal. Mach. Intell. 14 (2), 239–256.

Beyer, B., Sholukha, V., Dugailly, P.M., Rooze, M., Moiseev, F., Feipel, V., Jan, S.V.S., 2014. In vivo thorax 3d modelling from costovertebral joint complex kinematics. Clin. Biomech. 29 (4), 434–438.

Bruno, A.G., Bouxsein, M.L., Anderson, D.E., 2015. Development and validation of a musculoskeletal model of the fully articulated thoracolumbar spine and rib cage. J. Biomech. Eng. 137 (8), 081003.

Chen, H.-C., Wu, C.-H., Wang, C.-K., Lin, C.-J., Sun, Y.-N., 2014. A joint-constraint model-based system for reconstructing total knee motion. IEEE Trans. Biomed. Eng. 61 (1), 171–181.

Chen, X., Graham, J., Hutchinson, C., Muir, L., 2013. Automatic inference and measurement of 3d carpal bone kinematics from single view fluoroscopic sequences. IEEE Trans. Med. Imaging 32 (2), 317–328.

Culham, E.G., Jimenez, H.A., King, C.E., 1994. Thoracic kyphosis, rib mobility, and lung volumes in normal women and women with osteoporosis. Spine 19 (11), 1250–1255.

De Troyer, A., Kirkwood, P.A., Wilson, T.A., 2005. Respiratory action of the intercostal muscles. Physiol. Rev. 85 (2), 717–756.

Didier, A.-L., Villard, P.-F., Saadé, J., Moreau, J.-M., Beuve, M., Shariat, B., 2009. A chest wall model based on rib kinematics. In: Proceedings of the Second International Conference in Visualisation. IEEE, pp. 159–164.

Dworzak, J., Lamecker, H., von Berg, J., Klinder, T., Lorenz, C., Kainmüller, D., Seim, H., Hege, H.-C., Zachow, S., 2010. 3D reconstruction of the human rib cage from 2d projection images using a statistical shape model. Int. J. Comput. Assist. Radiol. Surg. 5 (2), 111–124.

Fleming, A.D., Philip, S., Goatman, K.A., Olson, J.A., Sharp, P.F., 2006. Automated microaneurysm detection using local contrast normalization and local vessel detection. IEEE Trans. Med. Imaging 25 (9), 1223–1232.

Gendrin, C., Furtado, H., Weber, C., Bloch, C., Figl, M., Pawiro, S.A., Bergmann, H., Stock, M., Fichtinger, G., Georg, D., et al., 2012. Monitoring tumor motion by real time 2d/3d registration during radiotherapy. Radiother. Oncol. 102 (2), 274–280.

Gill, S., Abolmaesumi, P., Fichtinger, G., Boisvert, J., Pichora, D., Borshneck, D., Mousavi, P., 2012. Biomechanically constrained groupwise ultrasound to ct registration of the lumbar spine. Med. Image Anal. 16 (3), 662–674.

Gilmartin, J., Gibson, G., 1986. Mechanisms of paradoxical rib cage motion in patients with chronic obstructive pulmonary disease. Am. Rev. Respir. Dis. 134 (4), 683–687.

Grenier, S., Parent, S., Cheriet, F., 2013. Personalized 3d reconstruction of the rib cage for clinical assessment of trunk deformities. Med. Eng. Phys. 35 (11), 1651–1658.

Hansen, N., 2006. The CMA Evolution Strategy: A Comparing Review. In: Towards a New Evolutionary Computation. Springer, pp. 75–102.

Heeger, D.J., 1992. Normalization of cell responses in cat striate cortex. Vis. Neurosci. 9 (02), 181–197.

Ito, H., Koshizuka, S., Akihiro, H., Keiichi, N., 2011. Rib cage motion model construction based on patient-specific ct images between inhalation and exhalation. Med. Imaging Technol. 29 (4), 208–214. doi:10.11409/mit.29.208.

Jarrett, K., Kavukcuoglu, K., LeCun, Y., et al., 2009. What is the best multi-stage architecture for object recognition? In: Proceedings of the IEEE Twelfth International Conference on Computer Vision. IEEE, pp. 2146–2153.

Lamecker, H., Wenckebach, T.H., Hege, H.-C., 2006. Atlas-based 3d-shape reconstruction from x-ray images. In: Proceedings of the Eighteenth International Conference on Pattern Recognition, 1. IEEE, pp. 371–374.

Le, Q.V., 2013. Building high-level features using large scale unsupervised learning. In: Proceedings of the IEEE International Conference on Acoustics, Speech and Signal Processing (ICASSP). IEEE, pp. 8595–8598.

Lunacek, M., Whitley, D., 2006. The dispersion metric and the CMA evolution strategy. In: Proceedings of the Eighteenth Annual Conference on Genetic and Evolutionary Computation. ACM, pp. 477–484.

Markelj, P., Tomaževič, D., Likar, B., Pernuš, F., 2012. A review of 3d/2d registration methods for image-guided interventions. Med. Image Anal. 16 (3), 642–661.

Murphy, K., Van Ginneken, B., Reinhardt, J.M., Kabus, S., Ding, K., Deng, X., Cao, K., Du, K., Christensen, G.E., Garcia, V., et al., 2011. Evaluation of registration methods on thoracic CT: the EMPIRE10 challenge. IEEE Trans. Med. Imaging 30 (11), 1901–1920.

Otake, Y., Armand, M., Armiger, R.S., Kutzer, M.D., Basafa, E., Kazanzides, P., Taylor, R.H., 2012. Intraoperative image-based multiview 2D/3D registration for image-guided orthopaedic surgery: incorporation of fiducial-based C-arm tracking and GPU-acceleration. IEEE Trans. Med. Imaging 31 (4), 948–962.

Otake, Y., Wang, A.S., Uneri, A., Kleinszig, G., Vogt, S., Aygun, N., Sheng-fu, L.L., Wolinsky, J.-P., Gokaslan, Z.L., Siewerdsen, J.H., 2015. 3D–2D registration in mobile radiographs: algorithm development and preliminary clinical evaluation. Phys. Med. Biol. 60 (5), 2075.

Otake, Y., Wang, A.S., Webster Stayman, J., Uneri, A., Kleinszig, G., Vogt, S., Khanna, A.J., Gokaslan, Z.L., Siewerdsen, J.H., 2013. Robust 3D-2D image registration: application to spine interventions and vertebral labeling in the presence of anatomical deformation. Phys. Med. Biol. 58 (23), 8535–8553.

Penney, G.P., Weese, J., Little, J.A., Desmedt, P., Hill, D.L., et al., 1998. A comparison of similarity measures for use in 2-D-3-D medical image registration. IEEE Trans. Med. Imaging 17 (4), 586–595.

Prince, J.L., Links, J.M., 2014. Medical Imaging Signals and Systems, (second ed.) Pearson Prentice Hall, Upper Saddle River, New Jersey.

Rasoulian, A., Rohling, R., Abolmaesumi, P., 2013. Lumbar spine segmentation using a statistical multi-vertebrae anatomical shape+ pose model. IEEE Trans. Med. Imaging 32 (10), 1890–1900.

Talbi, E.-G., 2009. Metaheuristics: From Design to Implementation, 74. John Wiley & Sons.

Tanaka, R., 2016. Dynamic chest radiography: flat-panel detector (FPD) based functional x-ray imaging. Radiol. Phys. Technol. 9 (2), 139–153.

Tanaka, R., Sanada, S., Sakuta, K., Kawashima, H., 2015. Quantitative analysis of rib kinematics based on dynamic chest bone images: preliminary results. J. Med. Imaging 2 (2), 024002.

van de Kraats, E.B., Penney, G.P., Tomazevic, D., Van Walsum, T., Niessen, W.J., 2005. Standardized evaluation methodology for 2-d-3-d registration. IEEE Trans. Med. Imaging 24 (9), 1177–1189.

Van Uitert, R., Bitter, I., 2007. Subvoxel precise skeletons of volumetric data based on fast marching methods. Med. Phys. 34 (2), 627–638.

Veldkamp, W.J., Karssemeijer, N., 2000. Normalization of local contrast in mammograms. IEEE Trans. Med. Imaging 19 (7), 731–738.

Villard, P.-F., Escamilla, P., Kerrien, E., Gorges, S., Trousset, Y., Berger, M.-O., 2014. Preliminary study of rib articulated model based on dynamic fluoroscopy images. In: Proceedings of the SPIE Medical Imaging, p. 90361Y.

Yokota, F., Okada, T., Takao, M., Sugano, N., Tada, Y., Tomiyama, N., Sato, Y., 2013. Automated CT segmentation of diseased hip using hierarchical and conditional statistical shape models. In: Proceedings of the International Conference on Medical Image Computing and Computer-Assisted Intervention, 190–197.